Journal of Materials Chemistry C

ROYAL SOCIETY OF CHEMISTRY

PAPER

View Article Online
View Journal | View Issue

Cite this: J. Mater. Chem. C, 2024, 12, 11938

Switching between upconversion luminescence imaging and therapy *in vitro* enabled by NIR excitation modulation of nanocomposites†

Yuan Jiang,‡[a] Yale Hong,‡[a] Yuan-Yuan Liu,[b] Yue Guan,[a] Junxun Zhou,[c] Haifang Wang *[b] and Lining Sun *[a]

Received 15th April 2024,
Accepted 27th June 2024

DOI: 10.1039/d4tc01535e

rsc.li/materials-c

Herein, we designed and synthesized a theranostics-integrated nanocomposite capable of switching between upconversion luminescence imaging and photothermal therapy (PTT)/photodynamic therapy (PDT)/NO gas therapy by changing the wavelength of near-infrared light irradiation. L-Arginine (L-Arg) and indocyanine green (ICG) were encapsulated within mesoporous polydopamine layers coated on upconversion nanoparticles (UCNPs) to obtain the final nanocomposite UCNPs@mPDA/ICG@L-Arg (named UPIL). Under 980 nm irradiation, UPIL exhibits excellent performance in upconversion luminescence imaging. Meanwhile, upon 808 nm irradiation, UPIL not only produces thermal energy for PTT but also directly generates reactive oxygen species for effective PDT, achieving a synergistic effect of PTT/PDT. Furthermore, ICG in UPIL can serve as an oxidant, reacting with L-Arg to produce NO for gas therapy, which can also improve the PDT effect through the generated NO gas. Notably, the simple and effective switching between imaging (excited at 980 nm) and therapy (irradiated at 808 nm) can be achieved by altering the exciting wavelength of the nanocomposite. This orthogonal mode minimizes damage to normal tissue cells. Hence, this versatile nanocomposite platform, designed for near-infrared light-driven upconversion luminescence imaging and tri-modal synergistic therapy, holds the potential for imaging-mediated synergistic therapy, showcasing promising prospects for tumor treatment.

1. Introduction

Cancer, regarded as a paramount threat to human health, has resulted in millions of global fatalities attributable to the uncontrolled proliferation and metastasis of cancer cells.[1,2] It is well known that early diagnosis and treatment will greatly increase the likelihood of cure for patients. Therefore, multi-nanomaterials with both imaging and therapeutic functions are receiving increasing attention.[3–5] Multifunctional diagnostic and therapeutic integrated nanocomposite systems, combining therapeutic methods with suitable medical imaging modalities, hold significant promise in enhancing the effectiveness of cancer diagnosis and treatment.

In recent years, phototherapy has emerged as a new approach to tumor treatment, garnering growing interest.[6,7] The primary advantages of phototherapies include their minimally invasive nature, tumor specificity, precise spatial localization, and low toxicity and side effects.[8] Phototherapy has evolved to encompass various modalities, such as photodynamic therapy (PDT),[9,10] photothermal therapy (PTT),[11,12] photoinduction chemotherapy,[13,14] and photoimmunotherapy (PIT).[15,16] Nevertheless, clinical trial outcomes indicate that PDT or PTT in isolation faces challenges in achieving optimal anti-tumor effects.[17,18] Consequently, the synergistic approach of combining PDT and PTT is recognized as a more effective strategy for cancer treatment. Furthermore, integrating PDT can overcome the heat tolerance exhibited by tumor cells in response to PTT mediated by heat shock proteins. This enhancement renders tumor cells more susceptible to heat, thereby augmenting the efficacy of PTT.[19,20] There remain certain challenges in fully harnessing the potential of PTT/PDT combination therapy, including absorption mismatch or energy transfer between photothermal agents and photosensitizers, toxicity associated with nano-platforms, and the intricacies of binding chemistry.[21,22] Therefore, developing a straightforward and effectively unified treatment strategy for PTT/PDT is crucial. Indocyanine green (ICG), a U.S. Food and Drug Administration-approved drug, can be excited by 808 nm radiation and generate both a photothermal effect and cytotoxic reactive oxygen species (ROS).[23,24] Thus, the

[a] Department of Chemistry, College of Sciences, Shanghai University, Shanghai 200444, China. E-mail: lnsun@shu.edu.cn
[b] Institute of Nanochemistry and Nanobiology, School of Environmental and Chemical Engineering, Shanghai University, Shanghai 200444, China. E-mail: hwang@shu.edu.cn
[c] School of Medicine, Shanghai University, Shanghai 200444, China

† Electronic supplementary information (ESI) available. See DOI: https://doi.org/10.1039/d4tc01535e

‡ Jiang Yuan and Hong Yale are co-first authors.

synergistic therapy of PTT/PDT can be achieved by using ICG alone as the PTT reagent and photosensitizer.

Gas therapy has garnered significant interest and has undergone extensive study due to its "green" treatment with minimal side effects.[25,26] Gas therapy involves the utilization of gases such as hydrogen sulfide (H_2S),[27,28] nitric oxide (NO),[29,30] and carbon monoxide (CO)[31,32] for therapeutic purposes. Among these gases, NO acting as an endogenous neurotransmitter, plays a regulatory role in various physiological processes,[33,34] including cardiovascular homeostasis, infection immune response, and angiogenesis. NO at low concentration acts as an effective P-glycoprotein regulator, helping to overcome multidrug resistance, while NO at high concentration exhibits cytotoxic effects, contributing to the eradication of tumor cells. The primary NO donors include L-arginine (L-Arg), *N*-diazene dioleic acid (NONOate), *S*-nitrosomercaptan (RSNO), *etc.*[35–38] However, the toxic byproducts of NONOate and the swift clearance of RSNO restrict their potential application *in vivo*. Comparatively, L-Arg, serving as a natural NO donor, exhibits robust NO generation capacity catalyzed by inducible NO synthase.[39] Consequently, with the assistance of NO, gas therapy is able to achieve effective treatment.

Over the past few years, a myriad of multifunctional nanomaterials based on lanthanide-doped upconversion luminescent nanoparticles (UCNPs) have been constructed for the diagnosis and treatment of various kinds of cancer.[40] UCNPs hold great promise in biomedical applications, including low cytotoxicity, narrow emission bands, low autofluorescence, and absence of photodamage.[41] Furthermore, the near-infrared (NIR) excitation light used for UCNPs offers enhanced tissue penetration depth at relatively low power density compared to UV/visible light, making the nanoparticles more advantageous for biomedical applications.[42] Therefore, there is a pressing need to devise effective strategies to integrating UCNPs with synergistic therapy for theranostics applications.

Here, we synthesized a UCNP-based theranostics nanocomposite, UCNPs@mPDA/ICG@L-Arg (donated as UPIL), to achieve upconversion imaging-guided PTT/PDT/NO gas therapy. The nanocomposite effectively enhances the antitumor therapeutic efficacy *in vitro* by combining L-Arg on the surface of UCNPs encapsulated with mesoporous polydopamine (mPDA) and assembling ICG molecules. It is noteworthy that a 980 nm laser is employed to activate upconversion luminescence for bioimaging purposes, whereas an 808 nm laser is utilized to activate the PTT/PDT/NO gas therapy tri-modal synergistic treatment. The function to switch between imaging and therapy simply by altering the excitation wavelengths represents an orthogonal activation approach, which can significantly minimize damage to normal tissue cells and enhance the feasibility of achieving tri-modal therapy guided by upconversion luminescence imaging.

2. Experimental section

2.1. Materials and reagents

All reagents and chemicals were obtained from commercial sources and used without further purification. Ultrapure water was used throughout. $YCl_3{\cdot}6H_2O$ (99.99%), $YbCl_3{\cdot}6H_2O$ (99.99%), $ErCl_3{\cdot}6H_2O$ (99.99%), 1-octadecane (ODE, 90%), oleic acid (OA, 90%), dopamine hydrochloride and hexadecyltrimethylammonium chloride (CTAC), methanol (CH_3OH, 99.5%), ethanol (CH_3CH_2OH, 95%), acetone (CH_3COCH_3, 95%), and cyclohexane (C_6H_{12}, 99.5%) were purchased from Sigma-Aldrich Co., Ltd. Sodium hydroxide (NaOH, 96%), ammonium fluoride (NH_4F, 98%), ammonia monohydrate ($NH_3{\cdot}H_2O$, 25–28%), indocyanine green (ICG, 75%), and L-arginine (L-Arg, >98%) were obtained from Aladdin Company. The WST-8 cell counting kit (CCK-8) was purchased from Dojindo Molecular Technologies, Inc. 96 well plates were obtained from Greiner Bio-One GmbH. D-Hanks solution was obtained from Gibco Inc. The live/dead cell staining kit was obtained from Invitrogen, USA. 1,3-Diphenylisobenzofuran (DPBF), 2′,7′-dichlorofluorescein diacetate (DCFH-DA), 4-amino-5-methylamino-2′,7′-dichlorofluorescein diacetate (DAF-FM DA), and the Griess reagent were purchased from Beyotime, China.

2.2. Synthesis of UCNPs@mPDA (named UP)

As reported in our previous literature,[43] $NaYF_4$:20% Yb,2% Er (named UCNPs) was synthesized using thermal co-precipitation. The as-prepared oleic acid-coated UCNPs (2 mmol) were dispersed in cyclohexane and set aside. Then, hexadecyltrimethylammonium chloride (CTAC) (0.1 g) was dispersed in 15 mL of pure water. Once the liquid became clear, UCNPs (2 mmol, 2 mL) were added and stirred for 12 hours. An aqueous solution of dopamine hydrochloride (10 mL, 2 mg mL^{-1}) was added dropwise to the dispersed UCNPs in cyclohexane. After stirring for 2 hours, $NH_3{\cdot}H_2O$ (100 μL, 14.8 M) was added to the dispersion, causing an immediate color change to brown, and was stirred for 24 hours. The resulting precipitate was collected by centrifugation (15 000 rpm, 10 minutes), and the templating agent CTAC was removed after washing the precipitate three times using a solution of ethanol : acetone = 2 : 1 (v : v). The obtained UCNPs@mPDA (UP) was dispersed in 10 mL of deionized water for future use.

2.3. Synthesis of UCNPs@mPDA@L-Arg (named UPL)

An aqueous solution of L-Arg (5 mL, 1 mg mL^{-1}) was added to the UCNPs@mPDA aqueous dispersion (5 mL) and stirred for four hours. The precipitate was collected by centrifugation (15 000 rpm, 10 min) and washed three times with deionized water. Then the obtained UCNPs@mPDA@L-Arg (UPL) was dispersed in deionized water (5 mL) for further use.

2.4. Synthesis of UCNPs@mPDA/ICG@L-Arg (named UPIL)

ICG solution (2 mL, 0.5 mg mL^{-1}) was added dropwise to the aqueous dispersion of UCNPs@mPDA@L-Arg (5 mL) in the dark and stirred for 16 h. The precipitate was collected by centrifugation (15 000 rpm, 10 min), washed three times with deionized water, and then dispersed in deionized water (5 mL), which resulted in the final nanocomposite UCNPs@mPDA/ICG@L-Arg (UPIL). Then, UPIL was packed in a brown glass bottle and placed in the refrigerator at 4 °C.

2.5. Characterization

Transmission electron microscopy (TEM, Thermo Scientific Talos L120C, Thermo Fisher, America) was used to obtain

topographic images of the synthesized materials. X-Ray photoelectron spectroscopy (XPS, Thermo Scientific K-Alpha+, Thermo Fisher, England) was performed for molecular structure and atomic valence analysis of the samples. Fourier transform infrared (FT-IR) spectroscopy (AVATAR 370 FT-IR, Nicolet, America) was used to evaluate the chemical structures, and the infrared spectrometer was available in the range of 4000–400 cm^{-1}. The upconversion luminescence spectra were recorded on an Edinburgh FS-5 fluorescence spectrometer equipped with a continuous 980 nm laser, MDL-III-980 nm, CNI laser (Changchun New Industry Photonics Co., Ltd, Changchun, China). UV-vis-NIR absorption spectra were obtained using a Shimadzu UV-2500 PC spectrometer. Zeta potentials were measured on a Zetasizer 3000HS analyzer manufactured by Malvern Instruments. The Nova 1000 nitrogen analyzer was applied to measure nitrogen (N_2) adsorption/desorption isotherms.

2.6. Photothermal effect of UPIL nanocomposites

To evaluate the *in vitro* photothermal conversion properties of UPIL, aqueous dispersions of UPIL at concentrations of 0, 50, 100, 200, and 400 μg mL^{-1} were separately placed in a cuvette and an 808 nm laser (0.7 W cm^{-2}) was used for irradiation for 10 minutes. Simultaneously, a thermocouple thermometer probe with an accuracy of 0.1 °C was positioned vertically just below the liquid surface of the cuvette to record temperature changes. The probe was positioned carefully to prevent direct illumination. The temperature displayed on the thermocouple thermometer was recorded every 10 seconds, and this measurement was repeated three times for each sample. Under the same conditions, we recorded the 400 μg mL^{-1} UPIL aqueous dispersion temperature change under irradiation with a laser of different power densities (0.1, 0.4, and 0.7 W cm^{-2}). The photothermal conversion efficiency of nanoparticles was estimated by continuously irradiating a 400 μg mL^{-1} aqueous nanoparticle dispersion with a laser at a wavelength of 808 nm for 600 seconds. The calculation of photothermal conversion efficiency was performed using the following formula:

$$\eta = \frac{hS(T_{max} - T_{surr}) - Q_{Dis}}{I(1 - 10^{-A_{808}})}$$

where S is the surface area, h is the heat transfer coefficient, T_{max} is the maximum temperature of the system, T_{surr} is the ambient temperature of the surroundings, Q_{Dis} is the heat generated by the absorption of light by the solvent, A_{808} is the absorbance of the material, and I is the power density of the 808 nm laser (0.7 W cm^{-2}).

2.7. ROS and NO generation measurement

The measurement of singlet oxygen ($^1O_2$) generation was conducted by using 1,3-diphenylisobenzofuran (DPBF). DPBF typically exhibits a characteristic absorption peak near 410 nm, and its intensity diminishes irreversibly upon interaction with $^1O_2$, indicating the presence of a photodynamic effect. To assess the $^1O_2$ generation capability, under light-avoidance conditions, 2 mL of UCNPs, UP, UPL, UPI, UPIL, and ICG (with a concentration of 400 μg mL^{-1}) were placed in a cuvette, respectively. After addition of 20 μL of DPBF to each cuvette, the UCNPs, UP, UPL, UPI, UPIL, and ICG were irradiated using an 808 nm laser (0.7 W cm^{-2}) for 0, 2, 4, 6, 8, and 10 minutes, respectively. The absorption curves of DPBF were obtained using a UV-visible spectrophotometer.

The Griess method was employed to determine the production of NO by UPIL nanocomposites. Initially, a NO standard curve was established. A series of $NaNO_2$ solutions with concentrations of 0, 20, 40, 60, 80, and 100 μM were prepared. In each case, 2.0 mL of the solution under examination was placed in a cuvette, followed by the addition of 50 μL of Griess reagent. After 5 minutes, the absorbance of the samples at 540 nm was measured, and a standard curve was generated. To assess the *in vitro* NO production ability of UPIL, 2.0 mL of aqueous UPIL dispersion at concentrations of 50, 100, 200, and 400 μg mL^{-1} was placed in a cuvette, respectively. Subsequently, 50 μL of Griess reagent was added, and the sample was irradiated using an 808 nm laser (0.7 W cm^{-2}) for 2, 4, 6, 8, 10, and 12 minutes under light-avoidance conditions. The absorption spectra were measured using a UV-visible spectrometer. Similarly, the absorption spectra of a 400 μg mL^{-1} UPIL aqueous dispersion were recorded under irradiation using lasers with different power densities (0.1, 0.4, and 0.7 W cm^{-2}) for 2, 4, 6, 8, 10, and 12 minutes.

2.8. *In vitro* cytotoxicity assay

HeLa cells were inoculated in 96-well plates at a density of 8.0×10^3 cells per well and incubated in a CO_2 incubator at 37 °C for 24 hours. Following the removal of the culture medium, the cells were incubated in the fresh medium (with 10% serum) containing varying concentrations (25, 50, 100, 200, and 400 μg mL^{-1}) of UP, UPL, and UPIL nanocomposites. The cells exclusively incubated in the culture medium (with 10% serum) were used as the control. After 24 hours of incubation, the old medium was discarded. Subsequently, 100 μL of 10% CCK-8 solution diluted with culture medium was added. Wells containing only CCK-8 solution without cells were designated as the blank group. The well plates were then incubated in the CO_2 incubator for approximately 1 hour, and the absorbance at 450 nm was measured using a microplate reader. Cell viability was calculated using the following formula:

$$\text{Cell viability (\% Contral)} = \frac{A_{(test)} - A_{(blank)}}{A_{(control)} - A_{(blank)}} \times 100\%$$

where $A_{(test)}$ is the absorbance of the cells exposed to different materials, $A_{(control)}$ is the absorbance of the control, and $A_{(blank)}$ is the absorbance of the well without cells.

2.9. *In vitro* ROS and NO detection

To assess the production of intracellular ROS, the 2′,7′-dichlorofluorescein diacetate (DCFH-DA) assay was employed. DCFH-DA is susceptible to oxidation by ROS, resulting in the formation of 2′,7′-dichlorofluorescein (DCF), which emits a strong green fluorescence. HeLa cells were inoculated in 96-well plates at a density of 8.0×10^3 cells per well and incubated in the CO_2 incubator at 37 °C for 24 hours. Following the removal of the culture medium, the fresh medium (with 10% serum) containing 400 μg mL^{-1} of UP, UPL, UPI, and UPIL was

added to wells, respectively, while cells cultured in the medium alone served as the control. Cells treated with 0.15% H_2O_2 for 30 minutes served as the positive control. After 4 hours of incubation, cells were irradiated using a laser for 5 minutes, and the old medium was discarded. Following a wash with D-Hanks, 100 μL of D-Hanks containing 10 μM of DCFH-DA was added to each well. The 96-well plates were placed at room temperature for 30 minutes away from light. Subsequently, the dye was discarded, and another wash with D-Hanks was performed to remove excess dye. Afterwards, 100 μL of D-Hanks was added to each well, and the cells were observed under an inverted fluorescence microscope (DMI3000, Leica, Germany). The testing conditions included an excitation wavelength of 488 nm and an emission wavelength of 525 nm.

To visualize the production of intracellular NO, the NO fluorescent probe 4-amino-5-methylamino-2′,7′-dichlorofluorescein diacetate (DAF-FM DA) was utilized. HeLa cells were initially treated with UPIL for 24 h, followed by staining with DAF-FM DA for 30 min. Subsequently, the cells underwent 808 nm laser irradiation (0.7 W cm^{-2}) for 0, 1, 3, 5, 10, and 15 minutes and were observed under an inverted fluorescence microscope.

2.10. Live/dead staining

To directly observe the cell-killing effects, a live/dead cell staining kit was employed. HeLa cells were inoculated in 96-well plates at a density of 8.0×10^3 cells per well and incubated in the CO_2 incubator at 37 °C for 24 hours. After this incubation period, the culture medium was removed, and 400 μg mL^{-1} of UP, UPL, UPI, and UPIL in culture medium (with 10% serum) were added to wells, respectively. The cells cultured in the medium alone served as the control, and cells treated with 0.15% H_2O_2 for 30 minutes were used as the positive control. After 24 hours of incubation, cells were irradiated with a laser for 5 minutes, and the old medium was discarded. Following a wash with D-Hanks, 100 μL of dyes (calcein-AM and propidium iodide (PI)) in the kit were added to each well. The 96-well plate was placed at room temperature for 30 minutes away from light. Subsequently, the dyes were discarded, and another wash with D-Hanks was performed to remove excess dyes. Afterwards, 100 μL of D-Hanks was added to each well, and the stained cells were observed under the inverted fluorescence microscope. For green fluorescence testing (live cells), the excitation wavelength was 495 nm, and the emission wavelength was 515 nm. For red fluorescence testing (dead cells), the excitation wavelength was 525 nm, and the emission wavelength was 635 nm.

2.11. *In vitro* upconversion luminescence imaging of UPIL

The potential application of UPIL *in vitro* upconversion luminescence imaging was investigated under a confocal laser scanning microscope (CLSM). HeLa cells were treated with UPIL at a concentration of 400 μg mL^{-1} for 6 h and then rinsed with PBS multiple times to remove excess nanoparticles. The upconversion luminescence signals were captured within the 500–700 nm range under 980 nm irradiation at a power density of 0.5 W cm^{-2}. All images were acquired under consistent instrumental conditions.

3. Results and discussion

3.1. Preparation and characterization of UPIL nanocomposites

With CTAC as a templating agent, a mesoporous polydopamine (mPDA) layer was modified onto the UCNP ($NaYF_4$:20% Yb,2% Er) surface, resulting in UCNPs@mPDA (UP). Subsequently, abundant L-arginine (L-Arg) functionalized the UP through a Michael addition or a Schiff base reaction, leading to UCNPs@mPDA@L-Arg (UPL). Ultimately, ICG was loaded into UPL through π–π stacking, resulting in the final multifunctional nanocomposite UCNPs@mPDA/ICG@L-Arg (UPIL). Scheme 1 illustrates the preparation process and proposed applications of UPIL nanocomposites. Under 980 nm laser irradiation, the nanocomposite enables to exhibit upconversion luminescence imaging capabilities. When exposed to an 808 nm laser, UPIL not only absorbs NIR to generate heat for PTT but also generates singlet oxygen ($^1O_2$) for PDT. Furthermore, the L-Arg in UPIL produces NO gas in the microenvironment of tumor cells, which enables NO gas therapy driven by 808 nm laser irradiation.

Fig. 1a displays the TEM image of monodisperse $NaYF_4$:20% Yb,2% Er upconversion nanoparticles (UCNPs), which exhibit a hexagonal phase structure with a size of approximately 24 nm. The self-polymerization of dopamine salt under alkaline conditions resulted in the formation of a core–shell structure of UP

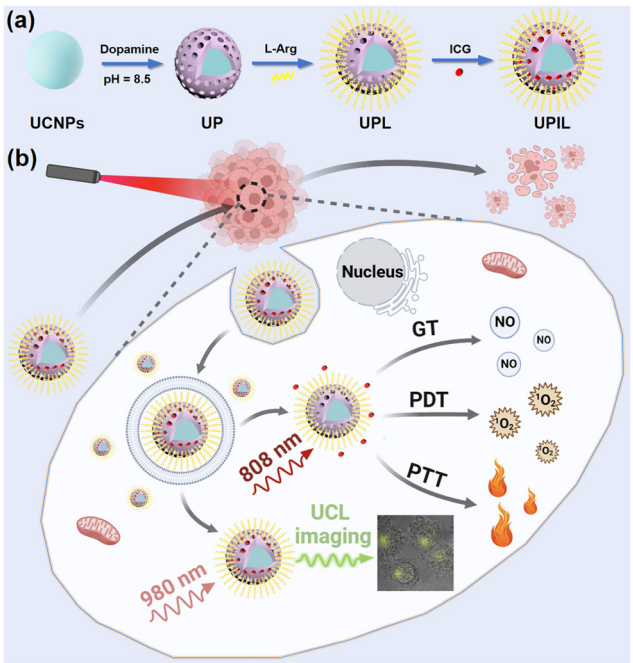

Scheme 1 (a) Synthesis of UCNPs@mPDA/ICG@L-Arg (UPIL) multifunctional nanocomposites and (b) the application research on triple-modal synergistic therapy and upconversion luminescence imaging in cancer cells. GT, PDT, and PTT stand for gas therapy, photodynamic therapy, and photothermal therapy, respectively.

by uniformly enveloping the UCNPs with a shell layer (Fig. 1b). The spherical UP particle shows a size of around 30 nm, suggesting the successful coating of UCNPs with a shell layer. Fig. 1c depicts the morphology of UPL modified by L-Arg. The morphology and structure of final nanocomposite UPIL are shown in Fig. 1d, maintaining the spherical structure with size being increased to about 35 nm and keeping good dispersity, which makes it suitable for cellular endocytosis.

Dynamic light scattering (DLS) measurements of UCNPs, UP, UPL, and UPIL are presented in Fig. S1 (ESI†). The UCNPs that dispersed in cyclohexane are well monodisperse, while UP, UPL, and UPIL dispersed in water have different degrees of agglomeration, as observed by the hydrated particle sizes of 141.9 nm, 214.7 nm, and 175.6 nm, respectively. This shows that UPL agglomerates more than UPIL does, which is due to a lower charge and lower electrostatic repulsion (Fig. S3, ESI†).

The FT-IR spectra of UCNPs, UP, UPL, and UPIL are presented in Fig. 2a. The characteristic peaks of UCNPs appear at 1562 and 1463 cm^{-1}, which are due to the asymmetric and symmetric stretching vibrations of carboxylate anions of oleic acid on the UCNPs surface, respectively. For the curve of UP nanoparticles, the characteristic peak at 1630 cm^{-1} is associated with N–H bending vibration, and the peak at 2923 cm^{-1} corresponds to the stretching vibration of C–H, which suggests the successful encapsulation of polydopamine. The characteristic peak at 1505 cm^{-1} in UPL arises from the characteristic stretching vibration of C═N, demonstrating successful modification by L-Arg.[44] The band at 1093 cm^{-1} in UPIL nanocomposites can be attributed to the stretching vibration of the vinyl group in ICG,[45] suggesting the loading of ICG in the final nanocomposite UPIL.

The surface composition and elemental valence analysis of UPIL nanocomposites were determined through X-ray photoelectron spectroscopy (XPS) tests. As shown in Fig. 2b, the XPS full spectrum reveals six distinct peaks at 688, 532, 399, 284, 168.5, and 159 eV, corresponding to elements of F, O, N, C, and S, respectively. The F element originates from UCNP nanoparticles, while the O, N, C, and S elements come from the mPDA shell layer, L-Arg, and ICG, demonstrating the successful preparation of UPIL. After peak-splitting fitting of the high-resolution XPS spectra of element C (Fig. S2a, d and g, ESI†), the three peaks at C–C (284.7 eV), C═C (284.1 eV), and C–N (285.4 eV) are assigned to mPDA, while the peak at C═N (286.9 eV) can be attributed to L-Arg and ICG. Compared with Fig. S2b and e (ESI†), the high-resolution XPS spectrum of element N (Fig. S2h, ESI†) displays a N═C peak, which is from ICG of UPIL. Additionally, the high-resolution XPS spectra of element S (Fig. S2c, f and i, ESI†) demonstrate that the S element derived from the sulfonic acid group of ICG ($-SO_3H$, 168.5 eV) only exists in UPIL (Fig. S2i, ESI†). Thus, it can be further deduced that the UPIL nanocomposite was successfully synthesized.

The changes in zeta potentials (Fig. S3, ESI†) of UP, UPL, UPI, and UPIL nanocomposites provide evidence for the successful synthesis of each material during the process. The potential value of mesoporous dopamine-modified upconversion nanoparticles UP was +13.27 mV, which changed to +2.48 mV after modification with negatively charged L-Arg. Finally, after further loading of ICG into UPL, the potential value changed to −15.39 mV (UPIL), supporting the successful creation of the final nanocomposites. In addition, the nitrogen adsorption–desorption curve of UP nanoparticles exhibits type IV isotherms (Fig. S4, ESI†), indicating the presence of a mesoporous structure. The specific surface area of UP nanoparticles is 33.69 $m^2\ g^{-1}$ determined using the Brunauer–Emmett–Teller (BET) method. This provides a theoretical foundation for the subsequent stacking loading of the ICG molecule.

Fig. 2c depicts the UV-visible-NIR absorption spectra of ICG, L-Arg, UP, UPI, UPL, and UPIL. The prominent absorption band of UPIL at around 808 nm is ascribed to the loading of ICG. This heightened absorption in the NIR region contributes to efficient photothermal conversion if irradiated by an 808 nm laser, thereby enhancing the photothermal therapeutic effects. Under 980 nm excitation, the upconversion emission spectra of UCNPs, UP, UPL, and UPIL are illustrated in Fig. 2d. They all show the three characteristic upconversion emissions at 525, 545, and 654 nm, attributed to $^2H_{11/2} \rightarrow {}^4I_{15/2}$, $^4S_{3/2} \rightarrow {}^4I_{15/2}$, and $^4F_{9/2} \rightarrow {}^4I_{15/2}$ transitions of Er^{3+} in the innermost core $NaYF_4$:Yb,Er, respectively. Although the successful coating of mPDA and the subsequent loading of L-Arg and ICG result in a corresponding reduction in the luminescence intensity of UPIL, the good upconversion emission property lays the foundation for subsequent cellular-level upconversion luminescence imaging from UPIL.

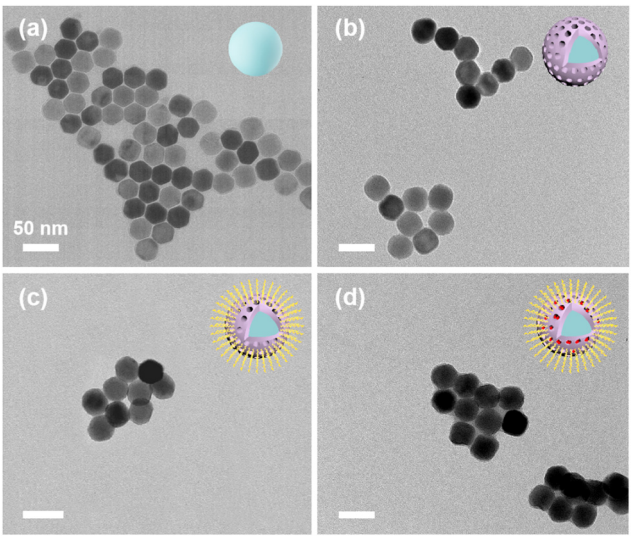

Fig. 1 Transmission electron microscopy (TEM) images of (a) $NaYF_4$:Yb,Er (named UCNPs), (b) UCNPs@mPDA (UP), (c) UCNPs@mPDA@L-Arg (UPL), and (d) UCNPs@mPDA/ICG@L-Arg (UPIL). Scale bar: 50 nm.

3.2. Photothermal conversion performance assay

Encouraged by broad absorption in the NIR region of nanocomposite UPIL (Fig. 2c), the photothermal conversion performance irradiated by 808 nm light was comprehensively assessed. Fig. 3a presents infrared thermal images captured at various concentrations of UPIL under continuous 808 nm laser irradiation (0.7 W cm^{-2}) for 0, 2, 4, 6, 8, and 10 minutes,

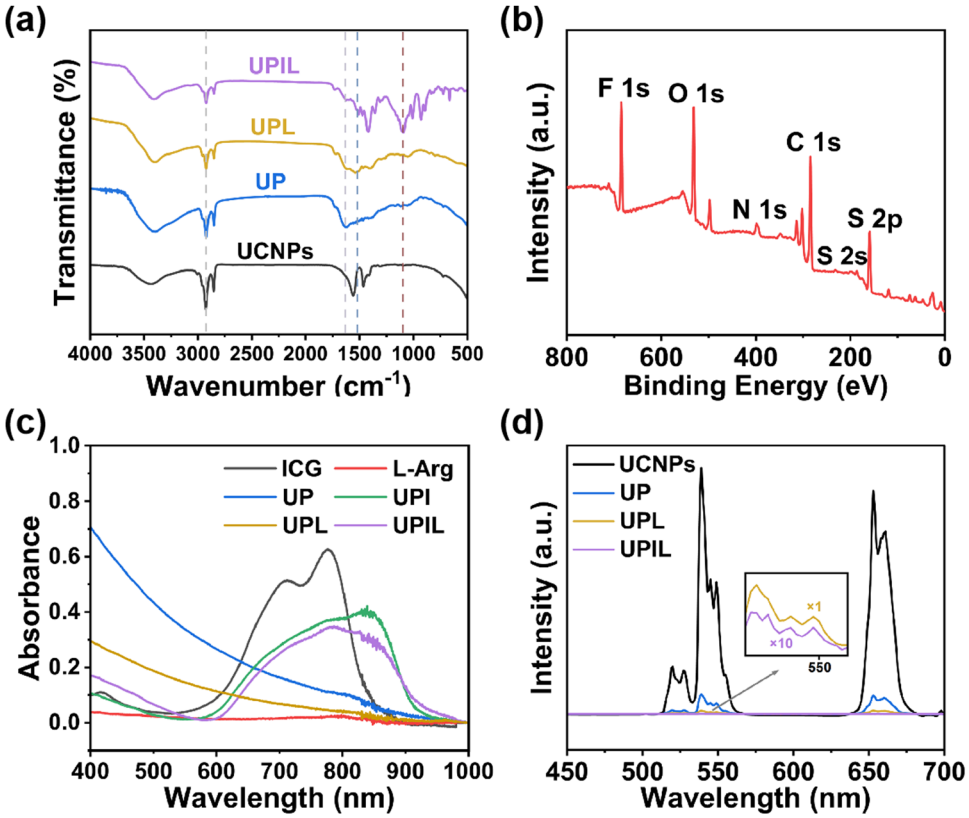

Fig. 2 Characterization of the as-prepared nanoparticles. (a) FT-IR spectra of UCNPs, UP, UPL, and UPIL. (b) X-ray photoelectron spectroscopy (XPS) of UPIL. (c) UV-vis-NIR absorbance spectra of ICG, L-Arg, UP, UPI, UPL, and UPIL, respectively. (d) Upconversion luminescence spectra (under an excitation of 980 nm) of UCNPs, UP, UPL, and UPIL, respectively.

respectively, illustrating that the photothermal conversion effect of UPIL is notably time-dependent and concentration-dependent. As illustrated in Fig. 3b, when the UPIL concentration was 400 μg mL^{-1}, the temperature of the UPIL aqueous dispersion increased rapidly over time, reaching about 45 °C, conducive to achieving conditions suitable for low-power photothermal treatment. For concentrations of 50, 100, and 200 μg mL^{-1} of UPIL, the temperatures increased to 24.5, 28.3, and 36.5 °C, respectively, while in the control group (deionized water), the temperature increased only slightly to 19.8 °C. Cancer cells initiate apoptosis at temperature above 42 °C, making UPIL at a concentration of 400 μg mL^{-1}, the selected treatment agent.

Additionally, the increase of temperature in the UPIL aqueous dispersion was not only related to the concentration but also closely linked to the irradiation power density used, indicating power density-dependent photothermal properties under 808 nm laser irradiation (Fig. 3c). The aqueous dispersion of 400 μg mL^{-1} UPIL was irradiated continuously for 10 minutes using an 808 nm laser with different power densities (0.1, 0.4, and 0.7 W cm^{-2}), respectively. The results show that the temperature of the UPIL aqueous dispersion increased more with time as the power density raised, reaching approximately 45 °C at 0.7 W cm^{-2}. Thus, 0.7 W cm^{-2} was chosen as the optimal power density for the final treatment.

To further investigate the photothermal conversion characteristics of UPIL (400 μg mL^{-1}), the nanocomposites were irradiated with an 808 nm laser (0.7 W cm^{-2}) for 10 minutes and then cooled down to room temperature (Fig. 3d) to examine the photothermal conversion efficiency. The value of τ_s was 287.97 s, and the photothermal conversion efficiency (η) of UPIL was determined to be 31.01% (Fig. 3e). These results indicate that the synthesized nanocomposite UPIL is a promising photothermal agent, providing data support for its subsequent cellular-level photothermal therapy.

3.3. ROS and NO generation

The production of singlet oxygen ($^1O_2$) from UPIL *in vitro* was assessed using 1,3-diphenylisobenzofuran (DPBF). As shown in Fig. 4a and b, when DPBF was introduced to the aqueous dispersion of UPIL and exposed to an 808 nm laser, the intensity at 410 nm decreased over time (0–10 min). Similarly, when the DPBF was added to a free ICG solution (Fig. S5a, ESI†) and UPI (Fig. S5b, ESI†), the corresponding absorption intensity at 410 nm decreased over time as well, as clearly illustrated through the curves of Fig. 4b. In addition, to demonstrate that the production of ROS is from ICG rather than UCNPs or L-Arg, we also carried out the assessment on UCNPs (Fig. S5c, ESI†), UP (Fig. S5d, ESI†), and UPL (Fig. S5e, ESI†) by using DPBF. The results indicate that it is ICG in the UPIL nanocomposite that can generate $^1O_2$ upon 808 nm laser irradiation, highlighting the potential of nanocomposites for effective photodynamic therapy.

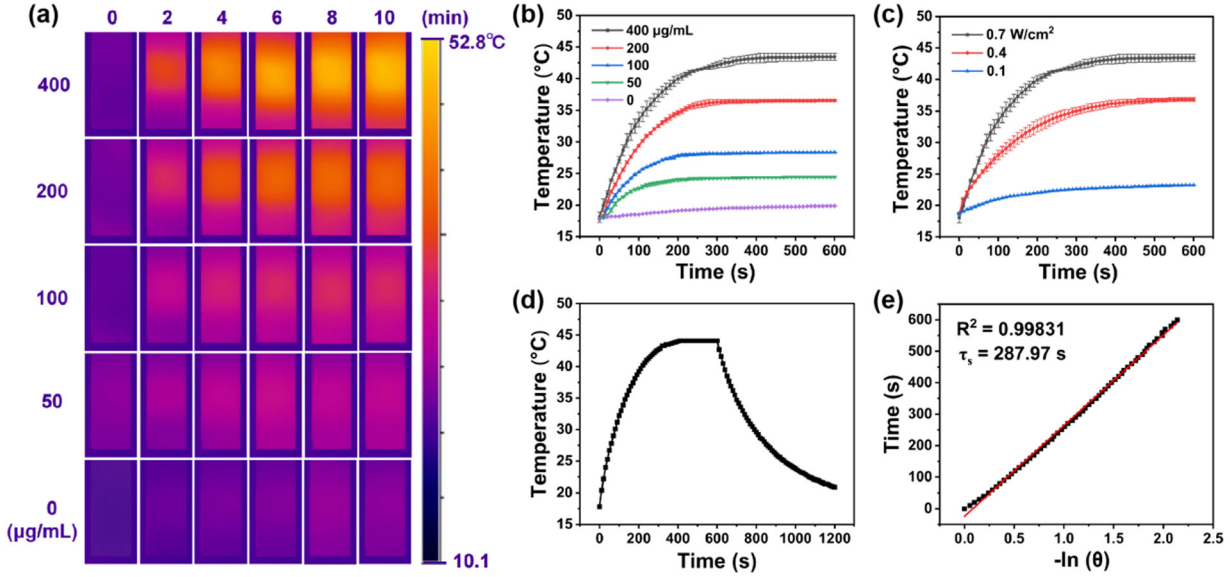

Fig. 3 Photothermal conversion performance of multifunctional nanocomposites UPIL. (a) Near-infrared thermal images of UPIL with different concentrations upon 808 nm laser irradiation with a power density of 0.7 W cm^{-2}. Water is set as the control group (0 μg mL^{-1}). (b) Temperature change curves of the UPIL aqueous dispersion with different concentrations (0, 50, 100, 200, and 400 μg mL^{-1}) upon 808 nm laser irradiation (0.7 W cm^{-2}) for 10 min. (c) Temperature change curves of the UPIL aqueous dispersion (400 μg mL^{-1}) upon 808 nm laser irradiation at different power densities (0.1, 0.4, and 0.7 W cm^{-2}) for 10 min. (d) Temperature change curves of the UPIL aqueous dispersion (400 μg mL^{-1}) were obtained by the power immediately closed after irradiation with an 808 nm laser for 10 min (0.7 W cm^{-2}). (e) The cooling time plot *versus* the negative natural logarithm of driving force temperature ($-\ln\theta$) with τ_s = 287.97 s for a concentration of 400 μg mL^{-1}.

The substantial production of ROS catalyzes the formation of NO from L-Arg. Consequently, the NO gas generated in response to ROS was measured using the Griess method, and the NO content in the samples was quantified based on the standard curve (Fig. S6, ESI†). The yield of NO from UPIL exhibited both concentration-dependent trends (Fig. 4c) and power-density-dependent characteristics (Fig. 4d) under 808 nm laser irradiation (0.7 W cm^{-2}). When 400 μg mL^{-1} of UPIL was irradiated for 12 minutes, the total NO yield achieved 12.17 μM. These results confirm that the synthesized UPIL can induce cascading photodynamic effects leading to ROS-dependent NO gas release.

3.4. *In vitro* cytotoxicity assay

The combined photothermal effect, the generation of substantial ROS, and the ROS-catalyzed NO release all induced by 808 nm NIR light are anticipated to synergistically induce cancer cell death. Thus, the cytotoxicity of the UPIL nanocomposite was first assessed using HeLa cells under the condition without NIR laser irradiation. As depicted in Fig. 5a, following co-incubation of HeLa cells with UP, UPL, and UPIL at concentrations ranging from 25 to 400 μg mL^{-1} in medium containing 10% serum for 24 hours, the cell viability exceeded 95% for UP and UPL across the concentration range. Moreover, the cell viability for UPIL at the dosages studied displayed an obvious decrease as the concentration of UPIL exceeded 200 μg mL^{-1}, yet remained above 85.1%. The low cytotoxicity makes the nanocomposite potentially useful for cell imaging *in vitro* and therapy in biomedical applications.

To further assess the treatment effect of UPIL nanocomposites on cancer cells, a live/dead cell assay was employed to directly visualize the status of HeLa cells. In this assay, live cells were stained green using calcein-AM, while dead cells were stained red using PI. As illustrated in Fig. 5b, the images of live and dead staining for HeLa cells treated by different samples (UP, UPL, UPI, and UPIL irradiated by an 808 nm laser at 0.7 W cm^{-2} for 5 minutes) were presented, respectively. Untreated HeLa cells served as the control group. No dead cells were observed in the control and the laser-only irradiation (NIR) group, indicating the safety of laser irradiation. After 808 nm laser irradiation for 5 minutes, a minimal number of dead cells were present in the UP and UPL groups. In contrast, with the addition of UPI and UPIL, both two images exhibit nearly complete cell death. These results suggest that UPIL holds promise as a potential candidate for multimodal therapy.

3.5. *In vitro* ROS and NO detection

Inspired by the extracellular ROS generation ability of UPIL nanocomposites, the potential to generating ROS in HeLa cells was further investigated. Intracellular ROS levels were assessed using the ROS probe DCFH-DA. Fig. 6 presents the fluorescence images of intracellular ROS in HeLa cells which were incubated with different materials (UP, UPL, UPI, UPIL) of 400 μg mL^{-1} for 4 hours and irradiated by an 808 nm laser at 0.7 W cm^{-2} for 5 minutes. Untreated HeLa cells were utilized as the control group, and HeLa cells treated with 0.15% H_2O_2 for 30 minutes served as a positive control (named POS). The ICG in UPIL was capable of producing ROS under 808 nm laser irradiation, as evidenced by strong green fluorescence observed in both UPI and UPIL groups upon laser irradiation after incubation with HeLa cells for 4 hours. It can be observed that green

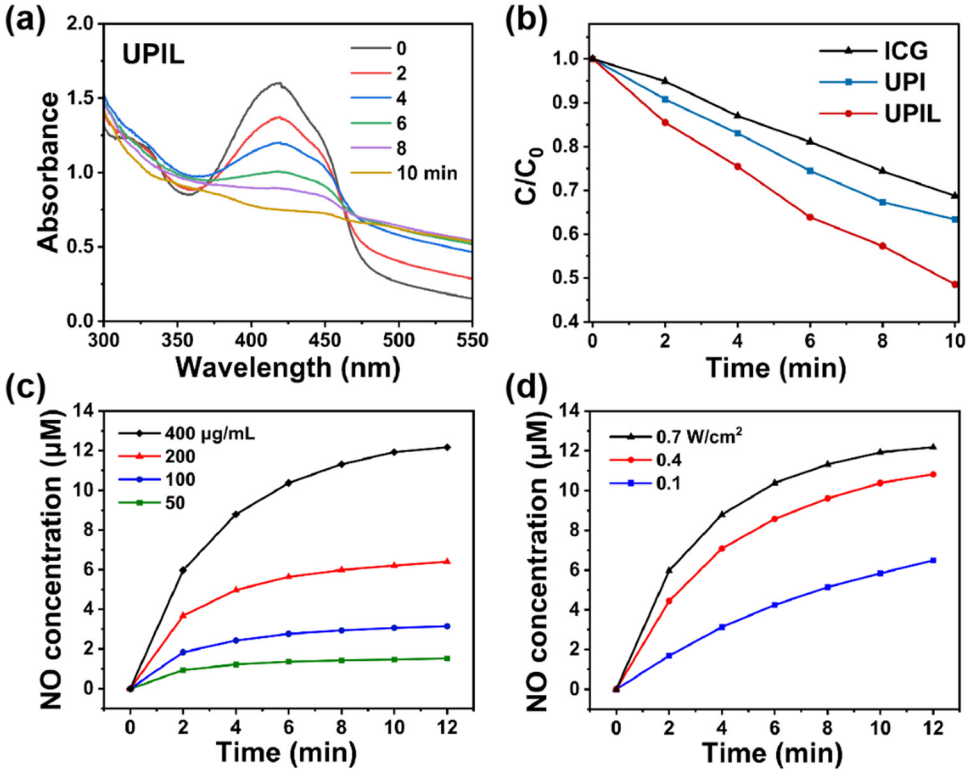

Fig. 4 (a) Time-dependent UV-absorbance spectra of UPIL (400 μg mL^{-1}) co-incubated with DPBF under 808 nm laser irradiation (0.7 W cm^{-2}, for 0, 2, 4, 6, 8, and 10 minutes, respectively). (b) Absorbance intensity at 410 nm of the DPBF solution co-incubated with different samples (ICG, UPI, and UPIL. Data from Fig. S5a, b, ESI,† and (a), respectively) as a function of time under 808 nm laser irradiation. (c) NO concentration change curves of the UPIL aqueous dispersion with different concentrations (50, 100, 200, and 400 μg mL^{-1}) upon 808 nm laser irradiation (0.7 W cm^{-2}) for 12 min. (d) NO concentration change curves of the UPIL aqueous dispersion (400 μg mL^{-1}) upon 808 nm laser irradiation with different power densities (0.1, 0.4, and 0.7 W cm^{-2}) for 12 min.

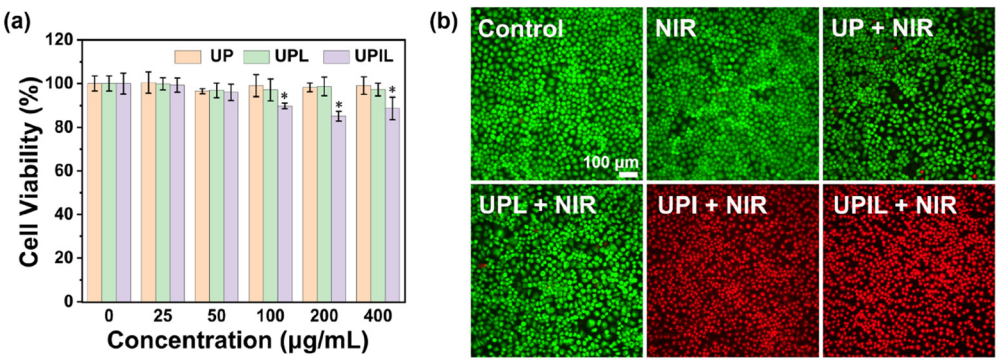

Fig. 5 (a) Cell viability of HeLa cells treated with UP, UPL, and UPIL nanocomposites at different concentrations (0, 25, 50, 100, 200, and 400 μg mL^{-1}) for 24 h. (*$p < 0.05$). (b) Live (green)/dead (red) staining of HeLa cells after different treatments (incubation with UP, UPL, UPI, or UPIL nanocomposites at the concentration of 400 μg mL^{-1} for 24 h, followed by 808 nm laser irradiation, 0.7 W cm^{-2}); the cells untreated are used as the control group. Scale bar: 100 μm.

fluorescence is more pronounced in the UPIL group compared to that in the UPI group, indicating that the presence of L-Arg could enhance ROS production. This is attributed to NO, which possesses a lengthy half-life (~5 s) and an extensive diffusion radius (40–200 μm), making it suitable for sensitizing PDT to enhance therapeutic efficiency.[46] In contrast, in both the UP and UPL groups without loading photosensitizer ICG, the intracellular fluorescence intensity is much lower, which suggests that less ROS was produced in these HeLa cells. The results demonstrate the potent ability of UPIL nanocomposites to generate ROS intracellularly, positioning them as promising candidates for photodynamic therapy.

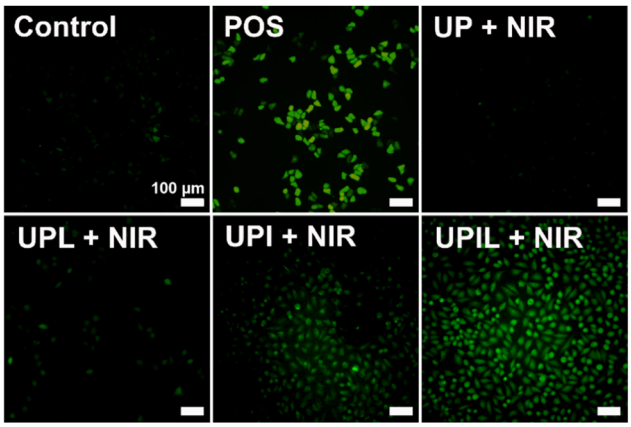

Fig. 6 Fluorescence images of intracellular ROS of HeLa cells after different treatments (incubation with 400 μg mL^{-1} UP, UPL, UPI, and UPIL nanocomposite for 4 h, followed by 808 nm laser irradiation for 5 min); the cells untreated are used as the control group, and those treated with 0.15% H_2O_2 for 30 min are used as the positive control (named POS). Scale bar: 100 μm.

Fig. 7 shows the visualization images of intracellular NO production after incubation with UPIL followed by staining with DAF-FM DA, upon 808 nm irradiation for different times. It can be seen that the intracellular NO signal gradually increases over time. Particularly, the signal was relatively small within initial 5 minutes and the cell morphology remained normal. A rounding of cell morphology occurred at 10 min, indicating the initiation of cell death. The cells were almost completely dead by the 15-min mark. These findings illustrate the time-dependent relationship between NO gas production and laser irradiation time, demonstrating the effective cancer cell-killing capabilities of NO gas treatment.

3.6. Upconversion luminescence imaging *in vitro*

Considering the excellent biocompatibility (Fig. 5a) and upconversion luminescence characteristics (Fig. 2d), the UPIL nanocomposites were incubated with HeLa cells for intracellular bioimaging study. Of importance is that the multimodal therapy investigation of UPIL was excited using an 808 nm laser, while upconversion luminescence imaging was achieved by 980 nm irradiation. The shift in laser irradiation wavelengths ensures the diagnosis and subsequent treatment of cancer. As shown in Fig. 8, HeLa cells were treated with UPIL for 6 hours at 37 °C, and upon excitation at 980 nm, the green emission and red emission of UPIL were collected at 500–600 nm and 600–700 nm, respectively. The results indicate that the nanocomposites exhibit robust upconversion luminescence without any autofluorescence signal in the cells. Hence, it can be reasonably deduced that UPIL nanocomposites can effectively penetrate into the HeLa cells and hold promise as effective candidates for upconversion luminescence imaging *in vitro*.

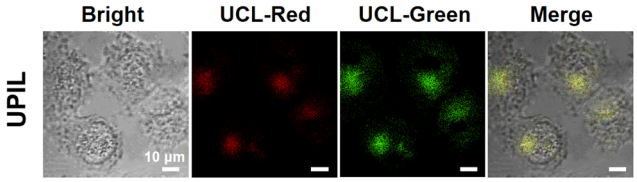

Fig. 8 Confocal laser scanning microscopy (CLSM) images of HeLa cells following incubation with 400 μg mL^{-1} UPIL for 6 h at 37 °C. The upconversion luminescence emission was collected by a green channel at 500–560 nm and a red channel at 600–700 nm; λ_{ex} = 980 nm, 500 mW. Scale bar: 10 μm.

4. Conclusions

In summary, we designed and synthesized UCN@mPDA/ICG@L-Arg nanocomposites, which display the capability of upconversion luminescence imaging (980 nm excitation) guided tri-modal PTT/PDT/NO gas synergistic therapy (808 nm excitation) *in vitro* by conversion of different NIR light irritation. Activated by a low-power 808 nm laser, the nanocomposite does efficiently convert light energy to heat, and the capacity to generate substantial ROS underscores its potential for effective photodynamic therapy. Furthermore, the introduction of L-Arg enables controlled NO gas release, showing promise for targeted NO gas therapy. Additionally, NO gas acts as a sensitizer, boosting the efficacy of photodynamic therapy. Orthogonal modes that vary the wavelength of excitation light can be used to switch the imaging-treatment modes and ensure the diagnosis and subsequent treatment of cancer. Thus, the developed nanocomposites put forward a useful method for the subsequent development of imaging diagnostic and multimodal therapeutic platforms under orthogonal excitation.

Data availability

The data that support the findings of this study are available in the ESI† of this article.

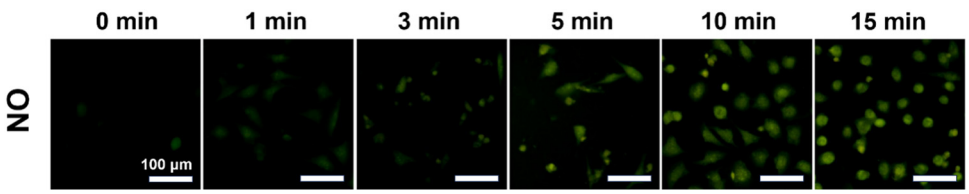

Fig. 7 Fluorescence images of intracellular NO production after incubation with UPIL followed by staining with DAF-FM DA, upon 808 nm irradiation (0.7 W cm^{-2}) for different times (0, 1, 3, 5, 10, and 15 min). Scale bar: 100 μm.

Conflicts of interest

The authors declare no conflict of interest.

Acknowledgements

We are grateful for the financial support from the National Natural Science Foundation of China (Grant No. 22275120) and the Science and Technology Commission of Shanghai Municipality (22520711600).

References

1 V. Shanmugam, S. Selvakumar and C.-S. Yeh, *Chem. Soc. Rev.*, 2014, **43**, 6254–6287.
2 K. D. Miller, L. Nogueira, T. Devasia, A. B. Mariotto, K. R. Yabroff, A. Jemal, J. Kramer and R. L. Siegel, *Ca-Cancer J. Clin.*, 2022, **72**, 409–436.
3 D. Liu, L. Liu, F. Liu, M. Zhang, P. Wei and T. Yi, *Adv. Sci.*, 2021, **8**, 2100074.
4 J. Shi, P. W. Kantoff, R. Wooster and O. C. Farokhzad, *Nat. Rev. Cancer*, 2017, **17**, 20–37.
5 R. Vankayala and K. C. Hwang, *Adv. Mater.*, 2018, **30**, 1706320.
6 D. E. J. G. J. Dolmans, D. Fukumura and R. K. Jain, *Nat. Rev. Cancer*, 2003, **3**, 380–387.
7 A. P. Castano, P. Mroz and M. R. Hamblin, *Nat. Rev. Cancer*, 2006, **6**, 535–545.
8 L. Song, B. Chen, Z. Qin, X. Liu, Z. Guo, H. Lou, H. Liu, W. Sun, C. Guo and C. Li, *Adv. Healthcare Mater.*, 2022, **11**, 2102298.
9 P. Kalluru, R. Vankayala, C. Chiang and K. C. Hwang, *Angew. Chem., Int. Ed.*, 2013, **52**, 12332–12336.
10 H. Liu, J. Li, P. Hu, S. Sun, L. Shi and L. Sun, *J. Rare Earths*, 2022, **40**, 11–19.
11 R. He, Y.-C. Wang, X. Wang, Z. Wang, G. Liu, W. Zhou, L. Wen, Q. Li, X. Wang, X. Chen, J. Zeng and J. G. Hou, *Nat. Commun.*, 2014, **5**, 4327.
12 S. T. Dibaba, Y. Xie, W. Xi, A. Bednarkiewicz, W. Ren and L. Sun, *J. Rare Earths*, 2022, **40**, 862–869.
13 J. Yuan, J. Liu, Q. Song, D. Wang, W. Xie, H. Yan, J. Zhou, Y. Wei, X. Sun and L. Zhao, *ACS Appl. Mater. Interfaces*, 2016, **8**, 24445–24454.
14 T. Wang, Q. Zhou, Y. Zhang, Y. Zheng, W. Wang, Y. Hou, G. Jiang, X. Cheng and X. Wang, *RSC Adv.*, 2016, **6**, 45652–45659.
15 H. Chen, P. Zhang, Y. Shi, C. Liu, Q. Zhou, Y. Zeng, H. Cheng, Q. Dai, X. Gao, X. Wang and G. Liu, *J. Nanobiotechnol.*, 2022, **20**, 61.
16 H. Kobayashi and P. L. Choyke, *Acc. Chem. Res.*, 2019, **52**, 2332–2339.
17 X. Liu, Y. Yang, X. Wang, X. Liu, H. Cheng, P. Wang, Y. Shen, A. Xie and M. Zhu, *J. Mater. Chem. B*, 2021, **9**, 6396–6405.
18 Z. He, L. Zhao, Q. Zhang, M. Chang, C. Li, H. Zhang, Y. Lu and Y. Chen, *Adv. Funct. Mater.*, 2020, **30**, 1910301.
19 Y. Sun, Y. Zhang, Y. Gao, P. Wang, G. He, N. T. Blum, J. Lin, Q. Liu, X. Wang and P. Huang, *Adv. Mater.*, 2020, **32**, 2004481.
20 B. Poinard, S. Z. Y. Neo, E. L. L. Yeo, H. P. S. Heng, K. G. Neoh and J. C. Y. Kah, *ACS Appl. Mater. Interfaces*, 2018, **10**, 21125–21136.
21 J. Shi, L. Wang, J. Gao, Y. Liu, J. Zhang, R. Ma, R. Liu and Z. Zhang, *Biomaterials*, 2014, **35**, 5771–5784.
22 U. S. Chung, J.-H. Kim, B. Kim, E. Kim, W.-D. Jang and W.-G. Koh, *Chem. Commun.*, 2016, **52**, 1258–1261.
23 Z. Sheng, D. Hu, M. Xue, M. He, P. Gong and L. Cai, *Nano-Micro Lett.*, 2013, **5**, 145–150.
24 P. Liu, C. Yue, B. Shi, G. Gao, M. Li, B. Wang, Y. Ma and L. Cai, *Chem. Commun.*, 2013, **49**, 6143–6145.
25 Q. He, *Biomater. Sci.*, 2017, **5**, 2226–2230.
26 I. Andreadou, E. K. Iliodromitis, T. Rassaf, R. Schulz, A. Papapetropoulos and P. Ferdinandy, *Br. J. Pharmacol.*, 2015, **172**, 1587–1606.
27 K. Módis, E. M. Bos, E. Calzia, H. Van Goor, C. Coletta, A. Papapetropoulos, M. R. Hellmich, P. Radermacher, F. Bouillaud and C. Szabo, *Br. J. Pharmacol.*, 2014, **171**, 2123–2146.
28 J. Kang, Z. Li, C. L. Organ, C.-M. Park, C. Yang, A. Pacheco, D. Wang, D. J. Lefer and M. Xian, *J. Am. Chem. Soc.*, 2016, **138**, 6336–6339.
29 A. W. Carpenter and M. H. Schoenfisch, *Chem. Soc. Rev.*, 2012, **41**, 3742–3752.
30 H. Zhou, H. Yan, Y. Hu, L. E. Springer, X. Yang, S. A. Wickline, D. Pan, G. M. Lanza and C. T. N. Pham, *ACS Nano*, 2014, **8**, 7305–7317.
31 Q. He, D. O. Kiesewetter, Y. Qu, X. Fu, J. Fan, P. Huang, Y. Liu, G. Zhu, Y. Liu, Z. Qian and X. Chen, *Adv. Mater.*, 2015, **27**, 6741–6746.
32 B. Wegiel, D. Gallo, E. Csizmadia, C. Harris, J. Belcher, G. M. Vercellotti, N. Penacho, P. Seth, V. Sukhatme, A. Ahmed, P. P. Pandolfi, L. Helczynski, A. Bjartell, J. L. Persson and L. E. Otterbein, *Cancer Res.*, 2013, **73**, 7009–7021.
33 S. Moncada and J. D. Erusalimsky, *Nat. Rev. Mol. Cell Biol.*, 2002, **3**, 214–220.
34 C. Bogdan, *Nat. Immunol.*, 2001, **2**, 907–916.
35 P. G. Wang, M. Xian, X. Tang, X. Wu, Z. Wen, T. Cai and A. J. Janczuk, *Chem. Rev.*, 2002, **102**, 1091–1134.
36 K. Zhang, H. Xu, X. Jia, Y. Chen, M. Ma, L. Sun and H. Chen, *ACS Nano*, 2016, **10**, 10816–10828.
37 F. Yang, P. Chen, W. He, N. Gu, X. Zhang, K. Fang, Y. Zhang, J. Sun and J. Tong, *Small*, 2010, **6**, 1300–1305.
38 W. Fan, N. Lu, P. Huang, Y. Liu, Z. Yang, S. Wang, G. Yu, Y. Liu, J. Hu, Q. He, J. Qu, T. Wang and X. Chen, *Angew. Chem., Int. Ed.*, 2017, **56**, 1229–1233.
39 S. Kudo and Y. Nagasaki, *J. Controlled Release*, 2015, **217**, 256–262.
40 X. Guo, L. Li, W. Jia, C. Zhang, W. Ren, C. Liu and Y. Tang, *ACS Appl. Mater. Interfaces*, 2024, **16**, 19926–19936.
41 X. Wang, R. R. Valiev, T. Y. Ohulchanskyy, H. Ågren, C. Yang and G. Chen, *Chem. Soc. Rev.*, 2017, **46**, 4150–4167.
42 V. J. Pansare, S. Hejazi, W. J. Faenza and R. K. Prud'homme, *Chem. Mater.*, 2012, **24**, 812–827.
43 X. Ge, L. Sun, B. Ma, D. Jin, L. Dong, L. Shi, N. Li, H. Chen and W. Huang, *Nanoscale*, 2015, **7**, 13877–13887.
44 Y.-L. Yu, J.-J. Wu, C.-C. Lin, X. Qin, F. R. Tay, L. Miao, B.-L. Tao and Y. Jiao, *Mil. Med. Res.*, 2023, **10**, 21.
45 P. Xue, M. Hou, L. Sun, Q. Li, L. Zhang, Z. Xu and Y. Kang, *Acta Biomater.*, 2018, **81**, 242–255.
46 X. Zhang, G. Tian, W. Yin, L. Wang, X. Zheng, L. Yan, J. Li, H. Su, C. Chen, Z. Gu and Y. Zhao, *Adv. Funct. Mater.*, 2015, **25**, 3049–3056.